AIAA JOURNAL
Vol. 45, No. 1, January 2007

Flow Patterns and Wake Structure of a Swept-Back Wing

S. C. Yen*
National Taiwan Ocean University, Keelung 20224, Taiwan, Republic of China
and
C. M. Hsu†
National Taiwan University of Science and Technology, Taipei 10672, Taiwan, Republic of China

DOI: 10.2514/1.24045

This work examines the characteristics of the flow patterns, velocity properties, and vortex shedding in the wake of a finite swept-back wing at low Reynolds numbers. The airfoil of the wing is a NACA 0012, and the sweep-back angle is 15 deg. The smoke-wire technique is used to visualize the flow patterns and evolution of vortex shedding. Five characteristic smoke-streak flow modes, namely, the *attached surface flow*, *instability wave in wake*, *vortical wake*, *separation from near leading edge*, and *bluff-body wake* are classified according to chord Reynolds numbers and angles of attack. Additionally, flow topologies of these surface flow modes and the time-dependent wake evolution processes are analyzed from the separatrices, alleyways, and critical points. Moreover, the velocity field around the wing section is quantified by the particle image velocimeter. Finally, the velocity vector field, streamline pattern, vorticity contour, turbulence kinetic energy, and frequency of these five flow modes are presented and discussed.

Nomenclature

b	=	span of airfoil, 30 cm
c	=	chord length of wing, 6 cm
d	=	length of wing-section projection on cross-stream plane
f	=	frequency of instabilities in wake region, Hz
Re_c	=	Reynolds number based on chord length of wing ($=u_\infty c/\nu$)
Re_d	=	Reynolds number based on cross-stream projection of wing section ($=u_\infty d/\nu$)
Ro_d	=	Roshko number of vortex shedding ($=fd^2/\nu$)
Sr_d	=	Strouhal number of vortex shedding ($=fd/u_\infty$)
t	=	evolution time, s
t^*	=	reduced time ($=tu_\infty/c$)
u	=	x component of local instantaneous velocity
u_∞	=	time averaged freestream velocity
u'	=	x component of fluctuating velocity
v	=	y component of local instantaneous velocity
v'	=	y component of fluctuating velocity
x	=	streamwise coordinate, originated from leading edge of wing model
y	=	spanwise coordinate, originated from leading edge of wing model
α	=	angle of attack
Λ	=	sweep-back angle
ν	=	kinetic viscosity of airstream
ρ	=	density of airstream

Introduction

THE shape of a wing plays a dominate role in determining the lift, mobility, and controllability of an aircraft. A swept-back wing can not only postpone the onset of shock waves, but also increase stability in a high-speed flight. On a swept-back wing, the flow speed geometrically perpendicular to the leading edge is less than the flight speed. This can significantly increase the critical Mach number and so can avoid or postpone the occurrence of shock waves. Therefore, adopting a swept-back wing can increase the maximum air speed and Mach number, as well as decrease drag and unfavorable effects at subsonic speeds. However, the pitch-up induced from the tip stall remains a significant problem in flight safety [1], particularly in the case of low air speed, for example, taking off and landing. The flow around a swept-back wing consists of several distinct spatial and temporal periodic phenomena and, therefore, relates to many significant steady/unsteady flow structure problems, such as the Kelvin-Helmholtz instability of the detached shear layer, the formation process and motion of bubbles, the instability of the unsteady flows, and vortex interactions in the wake.

The smoke-wire technique can visualize a fine smoke-streak flow structure. Mueller [2] and Batill and Mueller [3] pioneered this approach in separate studies. Swirydczuk [4] employed a thin airfoil and smoke-wire visualization method to explore how a single vortex and the vortex wakes interact with each other in a wind tunnel. Results of that study indicated that, under certain conditions, the vortex airfoil wake interaction incurs the formation of new vortices from the part of the wake positioned closely to the vortex. The vortices rotated in the direction opposite to that of the incident vortex following the formation. Gad-el-Hak and Ho [5] used a towing tank to investigate the time-dependent flow around delta and swept wings. They concluded that additional visualization experiments were required to further elucidate the topology of the complex velocity fields on different airfoils.

Experimental research on velocity properties originated with the work of Silverstein et al. [6], who measured the mean velocity profile in the wake and provided empirical relationships for the wake decay. Han and Lakshminarayana [7] adopted hot-wire anemometry and numerical prediction to study the mean velocity and turbulence structure of the near-wake flow of a NACA 0012 wing. The mean velocity, turbulence intensity, and Reynolds shear stress components across the wake in the far downstream region revealed the complex nature of the wake and its asymmetrical behavior. They summarized the following three findings of their work. 1) The mean velocity defect at the wake center falls when the incidence angle is increased. 2) The turbulent kinetic energy and shear stress rise on the suction side and fall on the pressure side, due to the influence of streamline curvature. 3) The streamline curvature, which arises from the nonzero incidence angle, significantly affects the profile of the mean velocity as well as the turbulence properties. Subaschander and Prabhu [8] evaluated the mean velocity, the three turbulent normal stresses, and the two Reynolds shear stresses using a hot-wire anemometer to probe the wake behind an infinite swept-back wing

Received 20 March 2006; revision received 28 July 2006; accepted for publication 1 August 2006.

*Assistant Professor, Department of Mechanical and Mechatronic Engineering; scyen@mail.ntou.edu.tw.
†Graduate Student, Department of Mechanical Engineering.

with a general aviation wing (GAW-2) airfoil section. According to their results, they found that the profiles of the mean velocity and Reynolds shear stress exhibit asymmetry near the trailing edge and seem to become symmetric within a shear distance of 60 trailing edge momentum thicknesses.

Topological approaches can be adopted to analyze and interpret the flow patterns developed from the smoke-wire visualization and velocity field. Many studies have described the separation patterns based on topological features. Johnson and Patel [9] studied the skin-friction topology of a semi-ellipsoid wing using visualization methods. Major changes in the topology demarcate divisions between general ranges designated as follows: symmetric, low, intermediate, and high incidences. As a function of incidence, the topological evolution is affected by the three-dimensional pressure gradients and the transition to turbulence. Huang et al. [10] studied the vortex evolution process on the suction surface of an impulsively started NACA 0012 wing in a towed water tank. The formation, evolution, and shedding processes of the vortex system on the suction surface were observed and analyzed by the streak images. Topological critical points, separatrices, and alleyways were used to explain the unsteady structure of the instantaneous streamline patterns, and thus verified the topological rule for the number of singular points.

The complex vortex on the wing surface stirs the stable vortex shedding in the wake of a swept-back wing. Zaman et al. [11] observed the low frequency oscillation of flow, indicating that the normal bluff-body shedding occurs at $Sr \approx 0.2$ during a deep stall ($\alpha \geq 18$ deg), where Sr and α denote the Strouhal number and angle of attack, respectively. However, a low frequency periodic oscillation was observed at the onset of static stall ($\alpha \approx 15$ deg), reducing the corresponding Strouhal number by an order of magnitude. Huang and Lin [12] examined the vortex shedding and shear-layer instability of a NACA 0012 wing, indicating that the evolution of the vortex shedding behind the airfoil at a low angle of attack is closely related to the behavior of the shear-layer instabilities. The low frequency shedding is superimposed by the high frequency shear-layer instability waves at high angles of attack. The plot of Reynolds number versus angle of attack domain exhibits the following characteristic vortex shedding modes: laminar, subcritical, transition, and supercritical.

The current work is motivated by the need to improve the low Reynolds number performance of guide vanes in the swirling generator of a burner. The results of this work can also be applied to the design of rotary blades of fans, wind-power generators, fluid mixers, etc. Additionally, this study largely focuses on the following objectives: 1) to study the flow pattern with smoke-wire methods, 2) to establish flow structures by conducting a topology analysis, 3) to measure the turbulent properties with the particle image velocimetry (PIV), and 4) to calibrate the shedding frequency of vortices in the wake with the visualization techniques. Finally, the results of this study are presented by the flow patterns, the topological critical point analysis, velocity characteristics, and unsteady flow structures in the wake.

Experimental Setup

Wind Tunnel: Visualization Configuration

Smoke-wire visualization was performed in a closed-return wind tunnel as illustrated in Fig. 1. The test section of the wind tunnel was 60 cm × 60 cm × 120 cm. The floor of the test section was made of a polished aluminum alloy plate, and three highly transparent acrylic panels were installed as the ceiling and side walls for photography and visualization. The operating velocity ranged between 0.56 and 33 m/s. Within this velocity range, the maximum turbulence intensity was below 0.2%, and the nonuniformity of the velocity profile across the cross section was lower than 0.5%. The velocity of the approaching flow was monitored by a pitot-static tube. The thicknesses of the boundary layers [13] were about 4.03 and 1.65 mm at freestream speeds of 5.0 and 30.0 m/s, respectively. An aluminum plate with sharp leading and trailing edges was placed at 50 mm above the floor of the test section to control the boundary layer thickness.

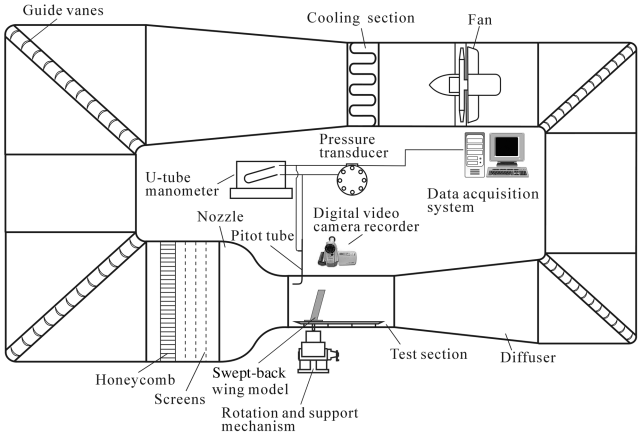

Fig. 1 Wind-tunnel configuration used for flow visualization.

Wind Tunnel: PIV Configuration

To exhaust the polyamide (PM) particles, the velocity property measurements were performed in an open-loop wind tunnel with a test section of 50 cm × 50 cm × 120 cm, as depicted in Fig. 2. Because the velocity of the swept-back wing is generally low in practical applications, the flow velocity in this wind-tunnel test section was regulated at 0.72 m/s. Because of the open loop and low speed operation, the flow velocity in the test section was very sensitive to the convection from the exterior environment. To prevent this disturbance, the exhaust section of the wind tunnel was specifically designed so that the stable operation range of 0.1–20.0 m/s was feasible with large exterior convection gusts. Notably, a lower limit of 0.05 m/s is possible in fair weather.

Airfoil Model

The airfoil model was manufactured from stainless steel. The profile of the cross section was NACA 0012 [14], and the sweep-back angle (Λ) was 15 deg. The chord length was 60 mm, and the wing span was 300 mm, yielding an aspect ratio of 5. The airfoil model was mounted on a support and protruded perpendicularly through the aluminum floor of the test section and the boundary layer thickness control plates.

Smoke-Wire Technique

The flow visualization was performed using two zigzag tungsten wires, which were placed in front of the leading edge and behind the trailing edge, respectively, at a distance of $x/c = 0.05$. The wire diameter was 0.2 mm. The zigzag structure was used to control the

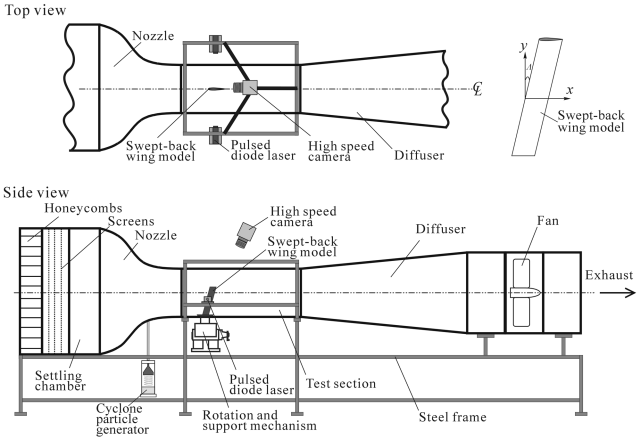

Fig. 2 Wind-tunnel configuration used for PIV measurement.

thickness and spacing of the smoke streaks. Thin mineral oil was brush coated onto the wire surface and electrically heated to create fine smoke streaks. The Reynolds number based on the smoke-wire diameter was maintained below 40 to prevent vortex shedding behind the wire [2]. The diameter of the aerosols of the condensed oil vapor, as measured by the Malvern 1600C laser particle analyzer, was 1.7 ± 0.3 μm. The Stokes number [15] of the oil aerosols was about the order of 10^{-3}, which is much lower than 1. Therefore, the smoke streaks were considered to follow the flow properly. Next, the smoke streaks were illuminated by a 0.6 mm-thick laser-light sheet on a symmetric plane. Two-dimensional streak images of the flow patterns were recorded on a computer at a rate of 30 frames/s (fps) via a CCD camera and a high-quality image grabber.

PIV Measurement

The PIV image acquisition system, as shown in Fig. 2, included two pulse-diode lasers, a high-speed camera, and a time synchronization control system. The laser beams from two lasers with the maximum power of 6 W were transmitted through an optical fiber and were then connected to a 20 deg laser-light sheet expander. The laser-light sheet expander was mounted onto the side rod of the outer steel frame so that the camera, test model, and laser-light sheet all moved in phase. The laser-light sheet was adjusted to about 0.5 mm thick and was aligned onto the midplane. For image grabbing, the particle images were recorded with a IDT Model XS-4 CCD camera with resolution of 512×512 pixels. The pixels were 16 μm square, and the system could be operated in continuous or external trigger mode. The pixel array was zoomed and mapped onto a physical region of around 13×13 cm^2, yielding a spatial resolution of about 254 μm/pixel. The maximum framing rate of the CCD camera was 5145 fps, and the exposure time was 0.2. Each frame comprised two interlaced video fields (even and odd) with a time interval of $1/5145$ s.

The PIV postprocessing system comprised an image interrogation and a postinterrogation system. Two consecutive image frames were analyzed with Keane and Adrian's cross-correlation technique [16], embedded in the VidPIV4 software from Optical Flow Systems. It determines the average displacement of local particle groups from the consecutive images. The interrogation window was 32×32 pixels. To lower the velocity bias in the regions of large velocity gradients, the displacement ratio of the double-exposed images to the length of the interrogation area was found to be smaller than the $1/4$ recommended by Keane and Adrian [17]. Filtering and interpolation were adopted to identify outliers and then regenerate the missed values. The global filter was applied to identify the global-inconsistent values, while the local filter was intended for identifying those that may be globally consistent but not smoothly consistent with the local variations in magnitudes and directions. The interpolation method is based on a weighted mean technique, which replaces the values at the filtered positions with an iterative process by replacing those with the most surrounding valid values first, working toward those that are least favorably positioned, to ensure accurate and reliable interpolation. Adaptive cross correlation, using small interrogation size and grid spacing, was finally applied to the vector field created from the regular procedure of cross correlation, filtering (global and local), and interpolation to provide higher resolution and accuracy than the first pass. A series of instantaneous vector fields was needed to obtain the ensemble averages. The mean velocity properties were obtained by combining a sufficient number of vector fields.

Error Analysis

In this work, alignment of the pitot tube and the calibration of the pressure transducer largely influenced the measurement accuracy of the freestream velocity. The uncertainty of freestream velocity with a synchronized micropressure calibration system and a careful alignment of the pitot tube was estimated as 3%. The accuracy of adjusting angle of attack was controlled within 0.5%. The uncertainty at the separation position was estimated to be below 4%.

The particle images were recorded by a IDT Model XS-4 CCD camera with a resolution of 512×512 pixels and a frame rate of 5145 Hz. The field of view, about 13×13 cm^2, corresponds to a spatial resolution of 254 μm/pixel. In the velocity interpolation process, the inverse-distance weighting algorithm

$$\tilde{V}_p = \frac{\sum_{k=1}^{N} W_k V_k}{\sum_k^N W_k} \tag{1}$$

was adopted for each velocity vector frame. In Eq. (1), $\tilde{V}_p$ denotes the interpolated velocity at node p; V_k represents the measured velocity, and W_k is the weighting function. This study applied a weighting function of $1/r^2$, where r represents the distance between the measured velocity V_k and the node being interpolated. According to Davis [18], Hart [19] and Huang et al. [10], the variance σ^2 of an interpolated velocity at node p can be approximated as

$$\sigma^2 = (\tilde{V}_p - V_p)^2 \approx \frac{\sum_{k=1}^{N} W_k \gamma(d_{kp})}{\sum_k^N W_k} \tag{2}$$

where the standard variance $\sigma = \sqrt{\sigma^2}$, and $\gamma(d_{kp})$ denotes the semivariance over a distance d_{kp}, which represents the separation between points k and p. The semivariance $\gamma(d_{kp})$ can be estimated as

$$\gamma(d_{kp}) = \frac{\sum(\tilde{V}_p - \tilde{V}_{p+d})^2}{2N} \tag{3}$$

which represents the sum of the squared differences between measured velocities ($\tilde{V}_p$, $\tilde{V}_{p+d}$) of pairs of points (N pairs in total) separated by the distance d_{kp}. Using this approximation, the ratios between the standard variances and the interpolated velocities (i.e., $\sigma/\tilde{V}_p$) are approximately 10–15%. This estimation of error is typically consistent with the analysis conducted by Spedding and Rignot [20], who adopted the weighting function $W_i = 1/r$.

Results and Discussion

Smoke-Streak Flow Patterns and Characteristic Flow Regimes

The smoke-wire technique was applied to visualize the detailed structure of complex flow phenomena. The flow separation as well as the vortex evolution can be visualized by combining the smoke-wire technique with a high-speed photography system and video recorder for wind velocities below 0.72 m/s. The flow patterns vary when fluid flows around the wing with various chord Reynolds numbers and angles of attack. The chord Reynolds number Re_c is defined as $Re_c = u_\infty c/\nu$, where ν denotes the kinematic viscosity of air; u_∞ denotes the freestream velocity, and c denotes the chord length of the airfoil. Figure 3 displays the typical smoke-wire visualization characteristic flow patterns on the $y/c = 0$ plane, where the tip and wall effects are insignificant. The surface separation and vortex bubble occur at different angles of attack when $Re_c = 2785$.

The laminar boundary layer on the upper and lower surfaces of the airfoil were all attached to the surfaces when $\alpha = 0$ deg, as shown in Fig. 3a. No trace of separation or vortical structures were observed on the wing surfaces. The flow smoothly left the upper and the lower surfaces of the airfoil at the trailing edge. Thus it satisfied the Kutta condition. Figure 3b illustrates a similar phenomenon when $\alpha = 2$ deg. This flow pattern is identified as the mode of *attached surface flow* at a low angle of attack.

The laminar boundary layer on the suction surface separated at about 95% chord when $\alpha = 6$ deg, as shown in Fig. 3c. The separation started from the trailing edge and moved toward the leading edge with increasing angle of attack. No reattachment of the separated boundary layer was found in this region. This type of surface boundary layer separation flow pattern is identified as the mode of *instability wave in wake*.

According to Fig. 3d, $\alpha = 15$ deg, a separation-induced recirculation is formed in the separation boundary layer due to the increase of vorticity induced from the reverse flow. Near the wake region and on the suction surface, the vortices have developed into a

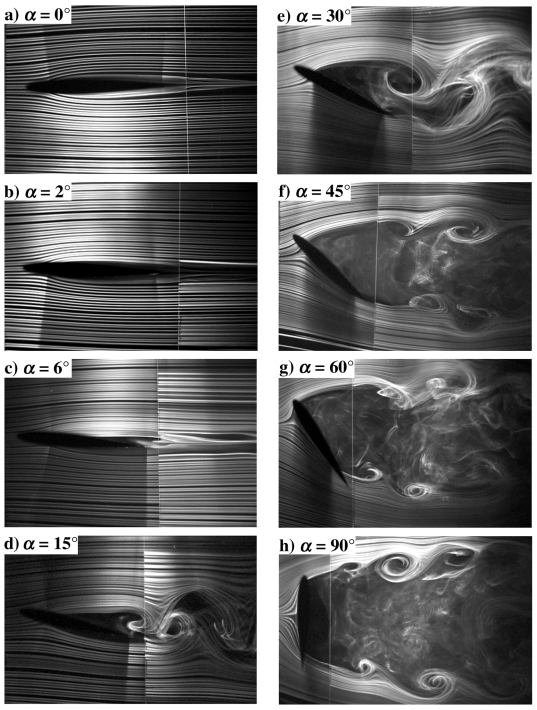

Fig. 3 Smoke-streak flow patterns on the suction surface at $Re_c = 2785$. Framing rate: 30 fps; exposure time: 1/6000 s.

paired structure, which looks like a Karman-type vortex street. This flow pattern is defined as a *vortical wake* mode.

As illustrated in Fig. 3e, $\alpha = 30$ deg, the separation point on the suction surface was very close to the leading edge, and the separation-induced recirculation disappears at high angles of attack. Furthermore, the weak turbulent momentum did not cause reattachment (Lissaman [21]). This flow pattern is defined as the mode of *separation from near leading edge*.

At extremely high angles of attack ($\alpha > 40$ deg), as revealed in Figs. 3f–3h, the shear layers on the suction and pressure surfaces moved away from the leading and trailing edges, respectively. Unstable waves induced from the separated shear layers developed to form the vortices. Because of the high angle of attack, the enlarged projected chord length removed the interaction between these two shear layers. The bluff-body effect incurred separations and strong pressure gradients and then produced vortex shedding in the wake. This flow pattern is named the *bluff-body wake* mode.

Figure 4 illustrates the correlations between the angle of attack (α) and the chord Reynolds numbers (Re_c). These flow regimes are categorized according to the particle-tracking flow patterns, as attached surface flow (type A), instability wave in wake (type B1), vortical wake (type B2), separation from near leading edge (type C), and bluff-body wake (type D). The fringes distinguishing these characteristic flow regimes bear some uncertainties. The maximum uncertainty was about ± 0.5 deg for α and ± 20 for Re_c, respectively.

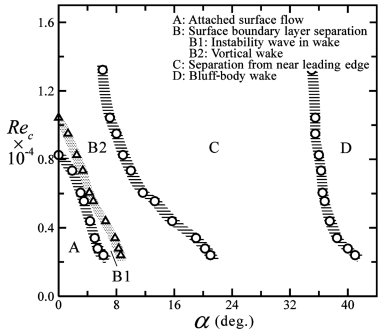

Fig. 4 Characteristic flow mode regimes.

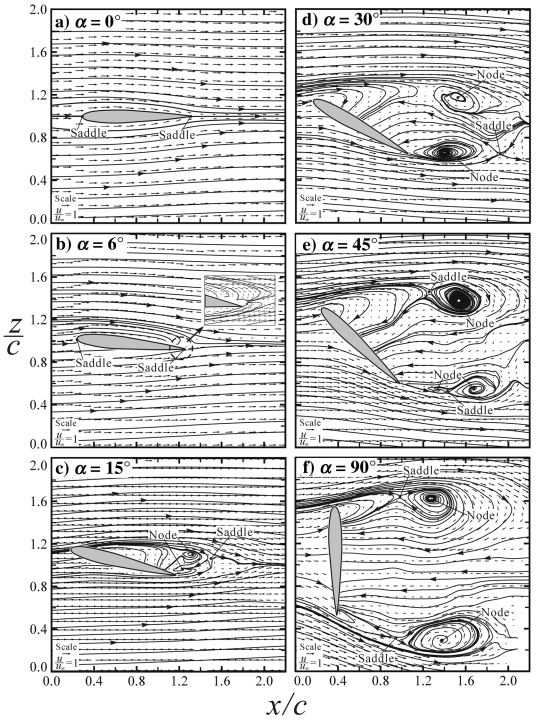

Fig. 5 Velocity vector fields and streamline patterns: a) attached surface flow mode, $\theta = 0$ deg; b) instability wave in wake mode, $\theta = 6$ deg; c) vortical wake mode, $\theta = 15$ deg; d) separation from near leading-edge mode, $\theta = 30$ deg; e) bluff-body wake, $\theta = 45$ deg; and f) bluff-body wake mode, $\theta = 60$ deg, respectively. $Re_c = 2785$.

Streamline Patterns, Vorticity, and Turbulent Kinetic Energy

All of the instantaneous streamline patterns, vorticity, and turbulent kinetic energy of the flowfields were quantitatively determined by PIV. Figures 5–7 display the typical instantaneous streamline patterns, vorticity, and turbulent kinetic energy contours changing with angles of attack when $Re_c = 2785$.

Streamline Patterns

Figure 5 shows the streamlines, which were derived from the vector plots obtained from the shooting method to delineate the detailed evolution processes of the flow structures. The figure clearly indicates that the sequence of vortex motions correlates with the streak photographs displayed in Fig. 3. In Fig. 5a, $\alpha = 0$ deg, the flow moved past both surfaces smoothly and therefore satisfied the Kutta condition. This plot does not display flow separation. The flow characteristic is similar to the behaviors of attached surface flow.

As shown in Fig. 5b, $\alpha = 6$ deg, flow separation occurred on the suction surface near the trailing edge. The inset indicates that back flow appeared at the trailing edge, and that no vortical structure appeared near the wake region. The flow structure is similar to the smoke steak patterns of instability wave in wake depicted in Fig. 3c.

In Fig. 5c, $\alpha = 15$ deg, the separation point on the suction surface moved toward the leading edge. Instability waves were formed in the shear layer on the suction surface and evolved further into vertical structures. These vortices were shed toward the wake region with time. This flow structure is similar to the vortical wake visualized in the smoke-streak patterns, as displayed in Fig. 3d.

The streamlines, in Fig. 5d, reveal that the separation point moved close to the leading edge when the angle of attack was further raised to 30 deg. This figure also exhibits a twin vortex in the wake region. This flow structure is similar to the separation from near leading edge in the smoke-streak flow pattern shown in Fig. 3e.

Figure 4 shows the flowfield when the angle of attack exceeded 40 deg, in which the flowfield exhibited the bluff-body wake mode. Additionally, shear layers on the suction and pressure surfaces were

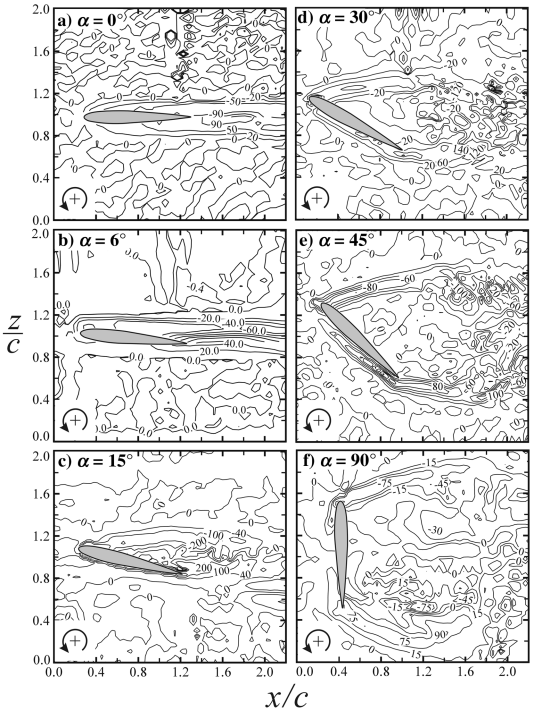

Fig. 6 Vorticity contours of flow: a) attached surface flow mode, $\theta = 0$ deg; b) instability wave in wake mode, $\theta = 6$ deg; c) vortical wake mode, $\theta = 15$ deg; d) separation from near leading-edge mode, $\theta = 30$ deg; e) bluff-body wake, $\theta = 45$ deg; and f) bluff-body wake mode, $\theta = 60$ deg, respectively. $Re_c = 2785$ for all cases.

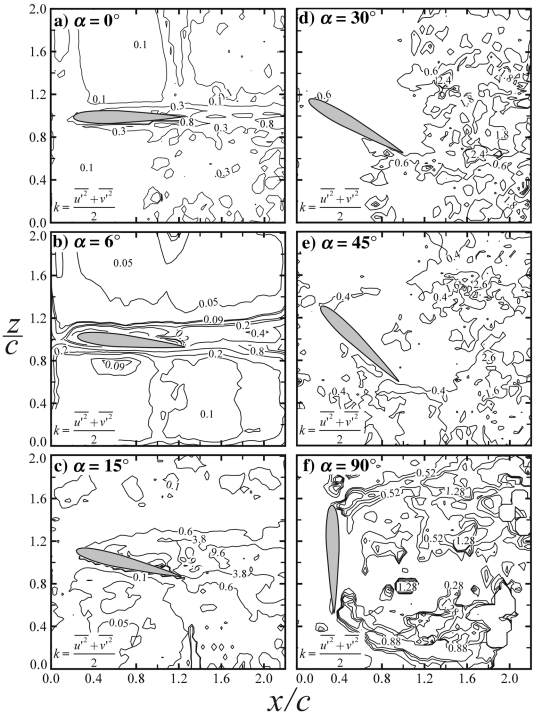

Fig. 7 Turbulent kinetic energy contours of flow: a) attached surface flow mode, $\theta = 0$ deg; b) instability wave in wake mode, $\theta = 6$ deg; c) vortical wake mode, $\theta = 15$ deg; d) separation from near leading-edge mode, $\theta = 30$ deg; e) bluff-body wake, $\theta = 45$ deg; and f) bluff-body wake mode, $\theta = 60$ deg, respectively. $Re_c = 2785$.

formed from the leading and trailing edges, respectively. Moreover, two vortices were formed separately from the shear layers on the suction and pressure surfaces. These two vortices then moved independently downstream. Figure 5e, $\alpha = 45$ deg, displays that two asymmetric vortices were formed independently. Figure 5f, $\alpha = 90$ deg, shows an almost symmetric vortex shedding pair resulting from the top and bottom shear layers. These two flow structures behave similarly to the smoke-streak patterns displayed in Figs. 3f and 3h.

Vorticity and Turbulent Kinetic Energy Contours

The vorticity Ω_z can be determined from the mean velocity data by the central difference scheme, which is defined as follows:

$$\Omega_z = \frac{\partial v}{\partial x} - \frac{\partial u}{\partial y} \tag{4}$$

In this study, a positive sign is defined as the vortex rotating counterclockwise. Figure 6 shows the vorticity strength distribution in this flowfield. The local maximum vorticities appeared at the nodes and saddle points. The distributions of two-dimensional turbulent kinetic energies derived from Fig. 5 are displayed in Fig. 7, and are defined as follows:

$$k = \frac{\overline{u'^2} + \overline{v'^2}}{2} \tag{5}$$

where u' and v' denote the velocity fluctuations in the x and y directions, respectively.

Figures 6a and 7a illustrate the distribution of vorticity and turbulent kinetic energy for the attached surface flow mode, respectively. Figure 6a indicates the maximum vorticity appearing in the wake and exhibits a symmetric but opposite vortex distribution. Figure 7a displays the distribution of the turbulent kinetic energy, which is similar to the vorticity contour.

Figures 6b and 7b, respectively, show the vorticity and turbulent kinetic energy contours for the mode of instability wave in wake. The boundary layer separated and formed the shear layer as the angle of attack rose. Near the shear layer, a negative vorticity was derived from the velocity gradient on the suction surface, while on the pressure surface, a positive vorticity was derived. Similar to the attached surface mode, these vorticities also exhibited a symmetric but opposite sign vorticity distribution, as depicted in Fig. 7b.

Figures 6c and 7c, respectively, show the vorticity and turbulent kinetic energy distributions of the vortical wake mode. The shear layers induced a staggered Karman-type vortex structure. A clockwise (negative) vortex was formed on the suction surface, while a positive (counterclockwise) vorticity was formed on the pressure surface. Figures 6d and 7d show the energy distributions of the separation from near leading-edge mode. A staggered Karman vortex structure was formed with the same mechanism as in the vortical wake mode.

For the bluff-body wake mode, the vorticity distributions are displayed in Figs. 6e and 6f, and the turbulent kinetic energy contours are shown in Figs. 7e and 7f. Because of the large pressure gradient induced from the rise in angle of attack, the vortex shedding was formed in the wake, and the vorticity strength was lowered due to the bluff-body effect.

Topological Analysis

Figure 8 shows sketches of the topological flow patterns. These topological sketches use the critical point theory, which was developed by Perry and Fairlie [22], Chong and Perry [23], and Lighthill [24]. Perry and Steiner [25] identified the sectional streamline patterns, which include the nodes (foci or centers), saddles, bifurcation lines, and their combinations by depicting the separatrices, critical points, and alleyways. This technique demonstrates the features of the flowfield, either the steady flow structures or the evolution process of unsteady vortical behaviors. Hunt et al. [26] developed a general formula, shown in Eq. (6), to describe the relationship between the numbers of nodes (including four-way nodes N and three-way nodes N') and saddles (including four-way saddles S and three-way saddles S') for flow moving around the surface obstacles:

$$(\Sigma N + 1/2\Sigma N') - (\Sigma S + 1/2\Sigma S') = 1 - n \qquad (6)$$

where n denotes the connectivity of the section of flow under consideration.

This study used these topological principles to analyze the swept-back wing at low chord Reynolds numbers. Figure 8 displays the flowfield topological characteristics as $Re_c = 2785$, and $n = 2$ for one obstacle in the flowfield. For the attached surface flow mode, Fig. 8a illustrates two three-way saddles, S_1' and S_2', occurring at the leading and trailing edges, respectively. These saddles satisfy the topological rule. Figure 8b displays the flowfield of surface boundary layer separation, which includes both the instability wave in wake and vortical wake modes. With the topological definitions, the specific numbers of points are listed as follows:

1) For the instability wave in wake mode: $\Sigma N = 2$, $\Sigma N' = 0$, $\Sigma S = 1$, and $\Sigma S' = 4$.

2) For the vortical wake mode: $\Sigma N = 3$, $\Sigma N' = 0$, $\Sigma S = 2$, and $\Sigma S' = 4$.

Equation (6) satisfies the topological rule when these values are substituted. The topological flow model shown in Fig. 8c represents the separation from near leading-edge mode. The critical points $\Sigma N = 4$, $\Sigma N' = 0$, $\Sigma S = 3$, and $\Sigma S' = 4$ were found to satisfy the topological rule. Figure 8d shows the topological flow pattern for the bluff-body wake mode with considering the bluff-body effect where $\Sigma N = 6$, $\Sigma N' = 0$, $\Sigma S = 5$, and $\Sigma S' = 4$.

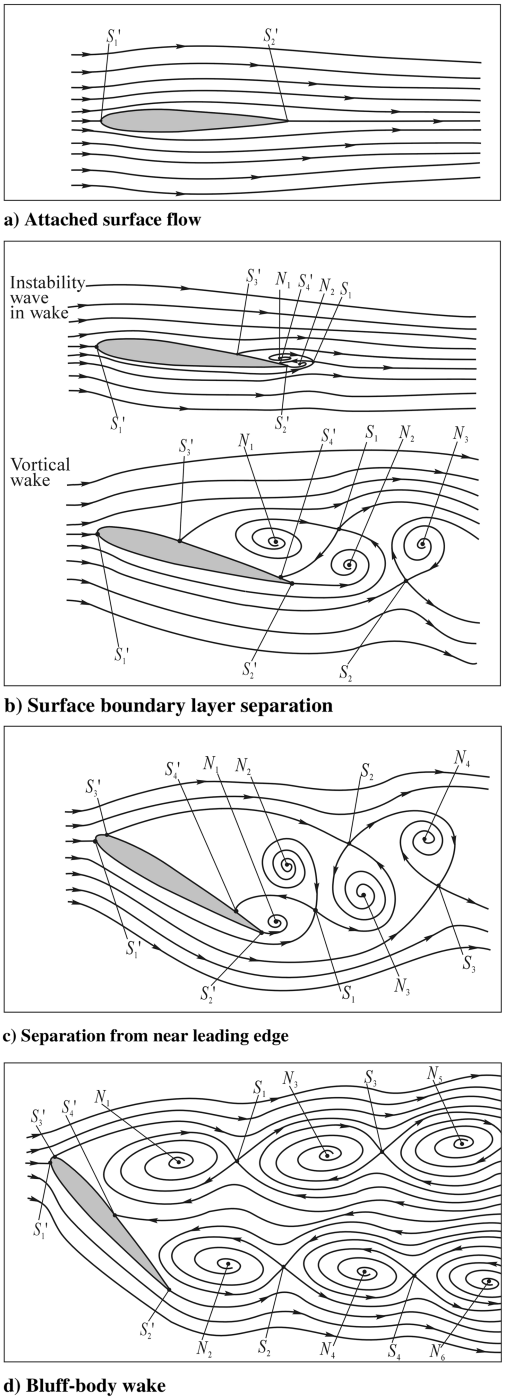

Fig. 8 Proposed topological flow structures: a) attached surface flow mode, $\theta = 0$ deg; b) instability wave in wake mode, $\theta = 6$ deg, and vortical wake mode, $\theta = 15$ deg; c) separation from near leading-edge mode, $\theta = 30$ deg; and d) bluff-body wake, $\theta = 45$ deg, respectively.

Wake Structure

This investigation applied the smoke wire to visualize the profile and planform views of flow structures in the wake on the plane of $y/c = 0$. Figures 9 and 10 display the results of this experiment at $Re_c = 2785$.

Profile View

Figure 9a demonstrates that the flow in the wake remained smooth and satisfied the Kutta condition. Figure 9b, $\alpha = 2$ deg, reveals the same phenomenon as $\alpha = 0$ deg. Figure 9c demonstrates unstable waves in the shear layer, in the region of $x/c > 4$ at $\alpha = 6$ deg. This figure indicates that the amplitudes of these unstable waves formed by the separation on the suction and pressure sides were amplified as they propagated downstream. As the angle of attack was increased, the boundary layer began to separate from the trailing edge on the suction side, and then a small phase difference was formed

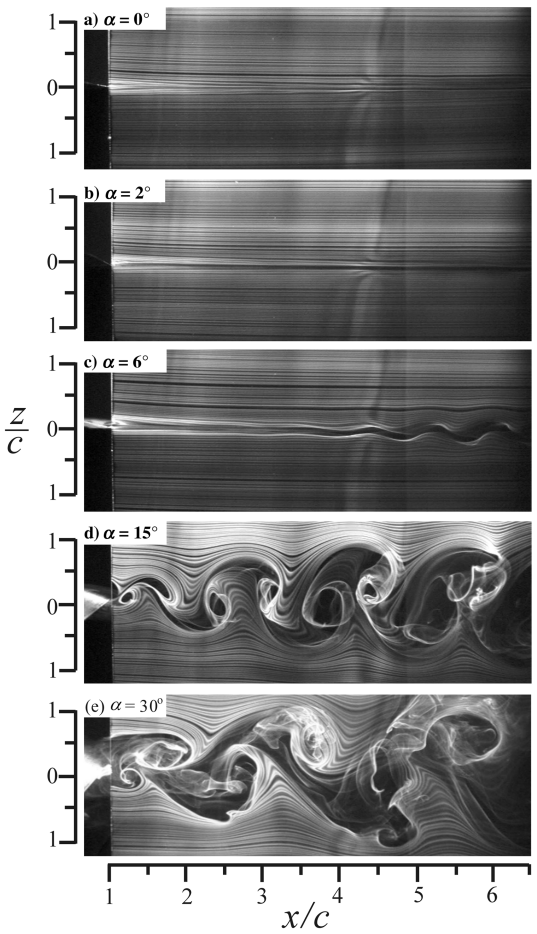

Fig. 9 Profile view of the smoke-streak visualization for unsteady swept-back flow structures in the wake region at $Re_c = 2785$. Framing rate: 30 fps; exposure time: 1/6000 s.

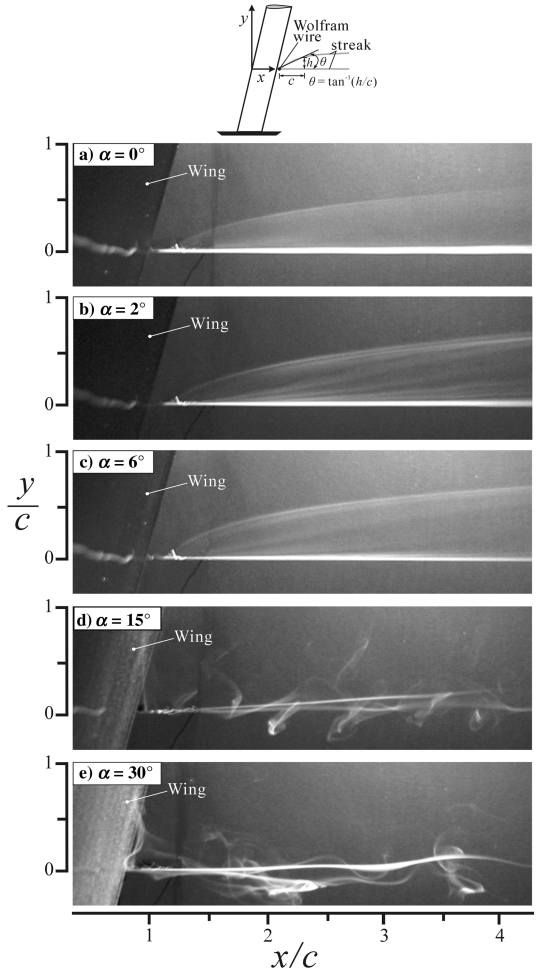

Fig. 10 Planform view of the smoke-streak visualization for unsteady swept-back flow structures in the wake region at $Re_c = 2785$. Framing rate: 30 fps; exposure time: 1/6000 s.

downstream. The instability waves moved to the trailing edge when the angle of attack was raised to $\alpha = 15$ deg, as shown in Fig. 9d. The alternatively shed Karman-type vortices were then formed near the trailing edge. The inceptive location of the Karman-type vortex shedding moved upstream, and its amplitude was amplified as the angle of attack increased. Figure 9e demonstrates the smoke-streak pattern at $\alpha = 30$ deg and indicates that the Karman coefficient was equal to 0.422. This coefficient represents the ratio of the longitudinal to the lateral spacing of the vortex pairs.

Planform View

This study also attempted to identify the flowfield properties along the chordwise and spanwise directions by adopting the smoke-wire visualization method at $Re_c = 2785$. Figure 10 displays the planform view of the smoke-streak flowfield near the trailing edge. Figure 10a illustrates the smoke-streak rise phenomenon at $\alpha = 0$ deg. The coherent chordwise and spanwise airspeed contributed to the occurrence of streak rising. Raising the angle of attack to lower the streamwise airspeed caused a larger rising angle, as shown in Fig. 10b. These two figures depict the features of the attached surface flow mode. The flow pattern became an unstable wave in the wake as the angle of attack rose further, while the smoke streak continued to rise, as depicted in Fig. 10c. The smoke streak rising disappeared when the angle of attack was greater than that of the vortical wake mode, as revealed in Figs. 10d and 10e. Figure 11 demonstrates that the rising angle θ was correlated with the chord Reynolds number. The symbol θ denotes the rising angle and is defined as the ratio of h to c, where c denotes the chord length, and h is the height of the rising smoke streak measured at the one chord length position of the horizontal smoke streak. Raising the angle of attack caused the rising

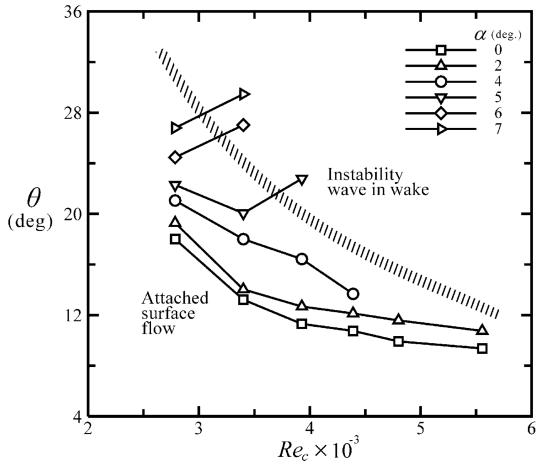

Fig. 11 Rising angle as a function of chord Reynolds number with various angles of attack.

angle to increase, while increasing the chord Reynolds number produced the opposite results. The unstable wave mode in the wake exhibited a larger increase in the rising angle when the angle of attack was raised.

Vortex Shedding

Evolution of Flowfield

To elucidate the evolution properties of the flowfield, this study focused on the separation from near leading-edge mode ($\alpha = 30$ deg), as illustrated in the regime C of Fig. 4. In this mode, the Karman-type vortex is formed on the airfoil surface. Figure 12 displays the evolution of these smoke-streak patterns. In this plot, the symbol t^* denotes the reduced time defined as $t^* = tu_\infty/c$, where t is the evolution time. Figure 12 displays periodic flow patterns captured from $t^* = 0.00$ to $t^* = 7.18$, respectively. The flow evolves back to the pattern at $t^* = 0.00$ when $t^* > 7.18$, completing the periodic cycle.

The flow patterns shown in Fig. 13 are discussed with topological theory. Figure 13a displays four nodes, three four-way saddles, and four three-way saddles in the flowfield. Inserting these values into the topological formula satisfies $(\Sigma N + 1/2\Sigma N') - (\Sigma S + 1/2\Sigma S') = -1$. As time evolved, Fig. 13b shows node N_1 convected out of the field of view, and the others shed downstream. Substituting these parameters into the topological formula, where $\Sigma N = 3$, $\Sigma N' = 0$, $\Sigma S = 2$, and $\Sigma S' = 4$, Eq. (6) is satisfied. Figure 13c displays a new node denoted as N_5, and these parameters become $\Sigma N = 4$, $\Sigma N' = 0$, $\Sigma S = 3$, and $\Sigma S' = 4$ to correspond with Eq. (6). In

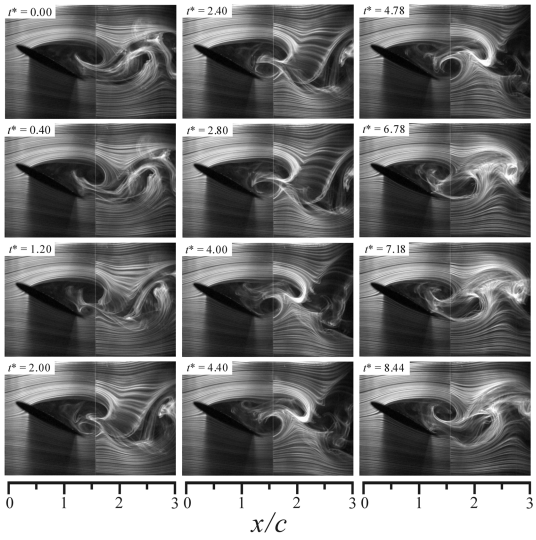

Fig. 12 Temporal and spatial evolution of velocity vectors and streamlines at $Re_c = 2785$ and $\alpha = 30$ deg.

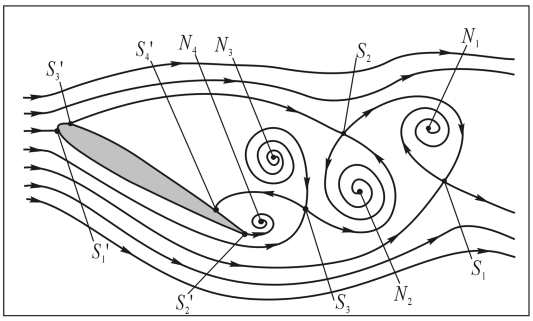

a) t^* = 0.00 ~ 2.00

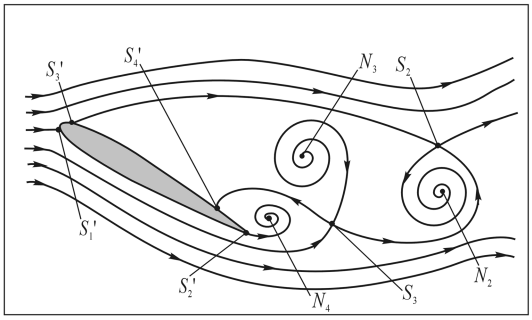

b) t^* = 2.00 ~ 4.00

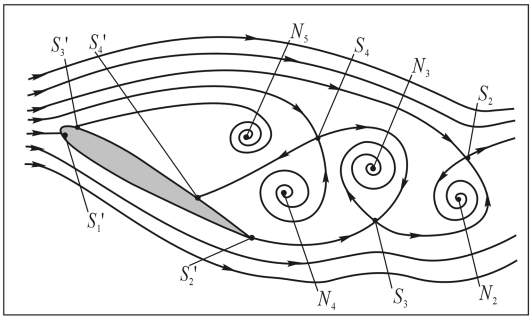

c) t^* = 4.00 ~ 6.78

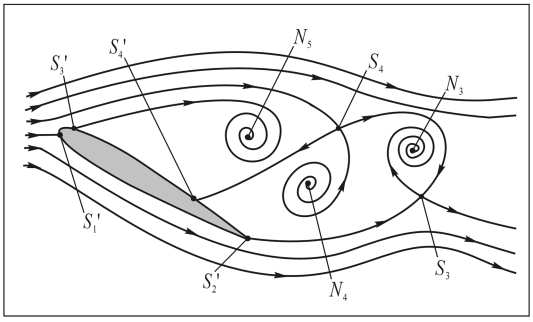

d) t^* = 6.78 ~ 7.18

(a)

Fig. 13 Proposed topological model for the separation from near leading-edge regime (type C).

Fig. 13d, node N_3 is pushed by node N_2 and then convected out of the field of view. The numbers of the saddles and nodes, $\Sigma N = 3$, $\Sigma N' = 0$, $\Sigma S = 2$, and $\Sigma S' = 4$, satisfies the topological formula [Eq. (6)]. Figures 12 and 13 indicate that the vortex shedding frequency $f = 1.67$ Hz.

Frequency of Vortex Shedding

Closely examining the dynamic behavior of the flow patterns in the wake reveals that the frequencies of unsteady motions of the

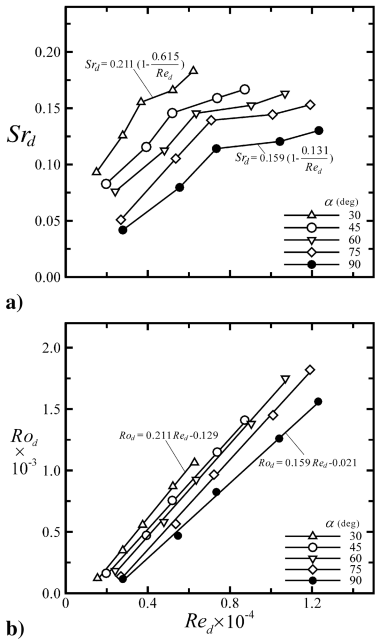

Fig. 14 a) Strouhal number Sr_d and b) Roshko number Ro_d as the functions of the projection Reynolds number Re_d, respectively.

swept-back wing can be normalized and represented by the nondimensional groups: projection Reynolds number $Re_d = u_\infty d/\nu$, projection Strouhal number $Sr_d = fd/u_\infty$, and Roshko [27] number $Ro_d = fd^2/\nu$, where ν denotes the kinetic viscosity of air, and d is the length projected to the freestream.

Roshko [27] has experimentally obtained a well-known equation for the nondimensional frequency Sr_d of the Karman vortex shedding in the wake with a circular cylinder:

$$Ro_d = 0.212Re_d - 2.7 \qquad 300 < Re_d < 2000 \tag{7a}$$

$$Sr_d = 0.212\left(1 - \frac{12.7}{Re_d}\right) \qquad 300 < Re_d < 2000 \tag{7b}$$

The Strouhal number of the cylinder wake approaches 0.212 when the projection Reynolds number is sufficiently large.

Figure 14 plots the relations between the Strouhal number and freestream velocities with various angles of attack. Figure 14a summarizes the experimental data that can be fitted by the following equations for $\alpha = 30$ deg and $\alpha = 90$ deg, respectively,

$$Sr_d = 0.211\left(1 - \frac{0.615}{Re_d}\right) \quad \text{for } \alpha = 30 \text{ deg} \tag{8a}$$

$$Sr_d = 0.159\left(1 - \frac{0.131}{Re_d}\right) \quad \text{for } \alpha = 90 \text{ deg} \tag{8b}$$

The results show that the Strouhal number decreases with increasing angle of attack.

For high angle of attack, the Roshko number increases with the projection Reynolds number, as shown in Fig. 14b. The Roshko number Ro_d is linearly related to Re_d and can be described as

$$Ro_d = 0.211Re_d - 0.129 \quad \text{for } \alpha = 30 \text{ deg} \tag{9a}$$

$$Ro_d = 0.159Re_d - 0.021 \quad \text{for } \alpha = 90 \text{ deg} \tag{9b}$$

The Strouhal number of the swept-back wing approaches 0.211 and 0.159 at $\alpha = 30$ deg and $\alpha = 90$ deg, respectively. Comparisons are made between the present results and those for an unswept wing presented by Huang and Lin [12]. The frequency characteristics of vortex shedding differ drastically between the swept-back and the

unswept wings. The maximum projection Strouhal numbers of the swept-back wing at $\alpha = 30$ deg and 90 deg exceed those of the unswept wing by about 24% and 27%, respectively. At $\alpha = 30$ deg, the Karman coefficient is 0.422, and the Strouhal number is 0.211. They satisfy the results of Levi's research [28].

Concluding Remarks

This study investigated the characteristics of flow patterns and wake structures on a NACA 0012 wing with a 15 deg sweep-back angle. Based on the results of this study, the following can be concluded:

1) The smoke-wire flow patterns are categorized into five characteristic flow regimes with changing the chord Reynolds number and angle of attack. These regimes are named the attached surface flow, the instability wave in wake, the vortical wake, separation from near leading edge, and the bluff-body wake, respectively.

2) The results of smoke-wire visualization can be determined and analyzed by PIV measurement and topological principle. Additionally, the quantified velocities and coordinate parameters can be used to find the vorticity and turbulent kinetic energy. The contour plots demonstrate distinct values near the airfoil surface and in the wake region.

3) The projection Strouhal number Sr_d is saturated and approaches 0.211 when the angle of attack is 30 deg. Regressing these data into the equation: $Sr_d = 0.211(1 - 0.615/Re_d)$, the Roshko number Ro_d is found to be linearly related to Re_d with the equation $Ro_d = 0.211Re_d - 0.129$.

4) The ratio of the Karman coefficient to the Strouhal number at $\alpha = 30$ deg is 2, which corresponds to that of the circular cylinder.

Acknowledgment

This research was supported by the National Science Council of the Republic of China, under Grant No. NSC 94-2212-E-019-006.

References

[1] Clancy, L. J., *Aerodynamics*, Wiley, New York, 1975, pp. 72–73.
[2] Mueller, T. J., "Flow Visualization by Direct Injection," *Fluid Mechanics Measurements*, 2nd ed., edited by R. J. Goldstein, Taylor & Francis, Washington, D.C., 2000, pp. 367–450.
[3] Batill, S. M., and Mueller, T. J., "Visualization of Transition in the Flow over an Airfoil Using the Smoke-Wire Technique," *AIAA Journal*, Vol. 19, No. 3, 1981, pp. 340–345.
[4] Swirydczuk, J., "A Visualization Study of the Interaction of a Free Vortex with the Wake Behind an Airfoil," *Experiments in Fluids*, Vol. 9, No. 4, 1990, pp. 180–190.
[5] Gad-el-Hak, M., and Ho, C. M., "Unsteady Vortical Flow Around Three-Dimensional Lifting Surface," *AIAA Journal*, Vol. 24, No. 5, 1986, pp. 713–721.
[6] Silverstein, A., Katzoff, S., and Bullivant, W., "Downwash and Wake Behind Plain and Flapped Airfoils," NACA Rept. 651, 1939.
[7] Han, C., and Lakshminarayana, B., "Measurement and Prediction of Mean Velocity and Turbulence Structure in the Near Wake of an Airfoil," *Journal of Fluid Mechanics*, Vol. 115, Feb. 1982, pp. 251–282.
[8] Subaschander, N., and Prabhu, A., "Turbulent Near-Wake Studies Behind an Infinitely Swept Wing," *Journal of Aircraft*, Vol. 39, No. 2, 2002, pp. 290–295.
[9] Johnson, T. A., and Patel, V. C., "Skin-Friction Topology over a Surface Mounted Semi-Ellipsoidal Wing at Incidence," *AIAA Journal*, Vol. 31, No. 10, 1993, pp. 1842–1849.
[10] Huang, R. F., Wu, J. Y., Jeng, J. H., and Chen, R. C., "Surface Flow and Vortex Shedding of an Impulsively Started Wing," *Journal of Fluid Mechanics*, Vol. 441, Aug. 2001, pp. 265–292.
[11] Zaman, K. B. M. Q., McKinzie, D. J., and Rumsey, C. L., "A Natural Low-Frequency Oscillation of the Flow over an Airfoil near Stalling Conditions," *Journal of Fluid Mechanics*, Vol. 202, May 1989, pp. 403–442.
[12] Huang, R. F., and Lin, C. L., "Vortex Shedding and Shear-Layer Instability of Wing at Low-Reynolds Numbers," *AIAA Journal*, Vol. 33, No. 8, 1995, pp. 1398–1430.
[13] Shames, I. H., *Mechanics of Fluid*, 3rd ed., McGraw–Hill, Singapore, 1992, p. 632.
[14] Abbott, I. H., and Von Doenhoff, A. E., *Theory of Wing Section*, Dover, New York, 1959, pp. 113–115.
[15] Flagan, R. C., and Seinfeld, J. H., *Fundamentals of Air Pollution Engineering*, Prentice–Hall, Englewood Cliffs, NJ, 1988, pp. 295–307.
[16] Keane, R. D., and Adrian, R. J., "Theory of Cross-Correlation Analysis of PIV Images," *Applied Scientific Research*, Vol. 49, No. 2, 1992, pp. 191–215.
[17] Keane, R. D., and Adrian, R. J., "Optimization of Particle Image Velocimeters Part 1: Double Pulsed Systems," *Measurement Science and Technology*, Vol. 1, No. 11, 1990, pp. 1202–1215.
[18] Davis, J. C., *Statistics and Data Analysis in Geology*, Wiley, New York, 1986, pp. 28–34.
[19] Hart, D. P., "PIV Error Correction," *Experiments in Fluids*, Vol. 29, No. 1, 2000, pp. 13–22.
[20] Spedding, G. R., and Rignot, E. J., "Performance Analysis and Application of Grid Interpolation Techniques for Fluid Flows," *Experiments in Fluids*, Vol. 15, No. 6, 1993, pp. 417–430.
[21] Lissaman, P. B. S., "Low Reynolds Number Airfoils," *Annual Review of Fluid Mechanics*, Vol. 15, 1983, pp. 223–239.
[22] Perry, A. E., and Fairlie, B. D., "Critical Points in Flow Patterns," *Advances in Geophysics B*, Vol. 18, 1974, pp. 299–315.
[23] Chong, M. S., and Perry, A. E., "A General Classification of Three-Dimensional Flow Fields," *Physics of Fluids A*, Vol. 2, No. 5, 1990, pp. 765–777.
[24] Lighthill, M. J., *Laminar Boundary Layers*, Oxford Univ. Press, Cambridge, England, U.K., 1963, pp. 48–88.
[25] Perry, A. E., and Steiner, T. R., "Large-Scale Vortex Structures in Turbulent Wakes behind Bluff Bodies. Part 1. Vortex Formation," *Journal of Fluid Mechanics*, Vol. 174, Jan. 1987, pp. 233–270.
[26] Hunt, J. C. R., Abell, C. J., Peterka, J. A., and Woo, H., "Kinematical Studies of the Flows Around Free or Surface-Mounted Obstacles; Applying Topology to Flow Visualization," *Journal of Fluid Mechanics*, Vol. 86, May 1978, pp. 179–200.
[27] Roshko, A., "On the Development of Turbulent Wakes from Vortex Streets," NACA Rept. 1191, 1954.
[28] Levi, E., "A Universal Strouhal Law," *Journal of Engineering Mechanics*, Vol. 109, No. 3, 1983, pp. 718–727.

F. Coton
Associate Editor